

Deep Model-Based Super-Resolution with Non-uniform Blur

Charles Laroche^{1,2}, Andrés Almansa², and Matias Tassano¹

¹GoPro France

²MAP5, CNRS & Université Paris Cité

Abstract

We propose a state-of-the-art method for super-resolution with non-uniform blur. Single-image super-resolution methods seek to restore a high-resolution image from blurred, sub-sampled, and noisy measurements. Despite their impressive performance, existing techniques usually assume a uniform blur kernel. Hence, these techniques do not generalize well to the more general case of non-uniform blur. Instead, in this paper, we address the more realistic and computationally challenging case of spatially-varying blur. To this end, we first propose a fast deep plug-and-play algorithm, based on linearized ADMM splitting techniques, which can solve the super-resolution problem with spatially-varying blur. Second, we unfold our iterative algorithm into a single network and train it end-to-end. In this way, we overcome the intricacy of manually tuning the parameters involved in the optimization scheme. Our algorithm presents remarkable performance and generalizes well after a single training to a large family of spatially-varying blur kernels, noise levels and scale factors.

1 Introduction

Single image super-resolution (SISR) methods aim to up-sample a blurred, noisy and possibly aliased low-resolution (LR) image into a high-resolution (HR) one. In other words, the goal of SISR is to enlarge an image by a given scale factor $s > 1$ in a way that makes fine details more clearly visible. The problem is ill-posed since there exist many ways to up-sample each low-resolution pixel. In order to further constrain the solution, a prior is usually imposed on the reconstructed HR output via a regularizer. Early Bayesian and variational approaches to the SISR problem used Tikhonov [40, 51], TV [1, 35], wavelet- ℓ_1 [15], non-local [44], or patch-recurrence [38, 39] regularization schemes, or adaptive filtering techniques [45] to impose a reasonable prior on the HR solution.

But classical regularization schemes have shown their limits. In order to cope with real world SISR problems, which are more ill-posed (higher noise levels, larger zoom factors, larger and more complex blur kernels) recent methods have turned to more powerful deep-learning-based regularizers, regressors or (conditional) generative models. And they succeeded remarkably,



Figure 1: Super-resolution with scale factor 2 in the presence of spatially-varying blur. The foreground is not blurred while the background is blurred using isotropic Gaussian kernel.

producing extremely high-quality results for very large ($\times 16$) scale factors, as long as blur is uniform and small [48].

The focus of this paper is on more realistic cases where blur kernels are non-uniform and much larger and complex, due mainly to motion blur and defocus blur [59, 67]. This particular case received much less attention in the recent deep-learning-based SISR literature. Among those recent works, only a few, including notably BlindSR [8], can handle non-uniform blur, and they do so only for relatively small and isotropic blur kernels that are quite far from real-world examples. And only a few of these works, including notably USRNet [63], can handle larger, anisotropic blur kernels like those arising in motion blur. This paper brings together these two characteristics to propose the first deep-learning based SISR method that can deal with both *spatially-varying* and *highly anisotropic, complex* blur kernels.

Like in [63] our architecture is an unfolded version of an iterative optimization algorithm that solves the underlying posterior maximization problem. As demonstrated in [63] this kind of model-based architecture provides a remarkable ability to generalize to a large family of blur kernels. In order to allow our architecture to deal with spatially-varying blur, while keeping computational complexity low, we derive the unfolding from a linearized version of the ADMM algorithm.

The rest of the paper is organized as follows: In Section 2 we review the recent SISR literature with an emphasis in their support for spatially-varying and highly-anisotropic blur kernels. Figure 2b summarizes our review which is later refined in Section 4.2. Section 3 introduces our architecture, its relationship to deep Plug & Play, and linearized ADMM algorithms and provides details on how our end-to-end architecture has been trained. The extensive experimental evaluation in Section 4 shows that our model significantly improves state-of-the-art performance on super-resolution with non-stationary blur, and that it can easily generalize to various non-uniform blur kernels, upscaling factors, and noise levels which is interesting for real-world applications. Training code and pre-trained model are available at: <https://anonymous.4open.science/r/NIMBUSR-0E27/README.md>

2 Related Work

2.1 Learning Based Super-Resolution

Several deep learning-based methods have been proposed to approach the SISR problem. SRCNN [11] is among the first models of this type. They employed a CNN to learn the mapping between an LR image and its HR version. Other methods used a similar approach but modified the architectures or losses [23, 24, 30, 52, 60]. ESRGAN [57] introduced a GAN based loss to reconstruct high-frequency details along with an architecture based on the Residual in Residual Dense Block (RRDB). ESRGAN generates sharp and highly realistic super-resolution on synthetic data. However, it struggles to generalize on real images, as their training dataset is built using bicubic downsampling. To overcome this limitation, BSRGAN [62] proposes to retrain ESRGAN on a more realistic degradation pipeline. Unlike previous SISR methods which disregard the blur kernel, SRMD [64] proposes to give the blur kernel information as an additional input to the network. This method then belongs to the family of so-called *non-blind* SISR methods. *Blind* methods such as [2, 8, 20] tackle the issue of kernel estimation for super-resolution using an internal-GAN, iterative kernel refinement or a dedicated discriminator. In [13, 50], the authors address the issue of generalization using an image-specific super-resolver trained using cyclic loss on intrinsic patches of the low-resolution image. Recently, SwinIR [28] proposes a swin transformer [34] based architecture that achieves state-of-the-art results while heavily reducing the number of parameters of the network.

2.2 Deep Plug-and-Play

Deep plug-and-play methods can be traced back to [55] where the image restoration problem is solved using ADMM optimization by decoupling the data and regularization terms. Then, they use a denoiser to solve the regularization sub-problem. This idea has been extended to other optimization schemes such as primal-dual methods [21, 36] or fast iterative shrinkage algorithm [22]. A large diversity of denoisers have been used for the regularization. Among them, BM3D has been used the most [9, 21, 22], but more recently deep CNN based denoisers have become very popular [36, 54]. [61] provides an analysis of the efficiency of the different deep denoisers for different image restoration tasks. Deep plug-and-play methods can be used to solve a large variety of image restoration tasks such as Gaussian denoising [5], image deblurring [58] or super-resolution [4]. Theoretical aspects of deep plug-and-play algorithms have also been studied using bounded denoisers assumptions [7] or more recently using denoisers whose residual operators are Lipschitz-continuous [26, 47]. More recently, [63] built a deep unfolding network called USRNet for super-resolution using deep plug-and-play optimization.

2.3 Spatially-Varying Blur

Removing uniform blur is a well-studied problem. Classical methods design natural image priors such as ℓ_1 [27], ℓ_2 [46] or hyper-Laplacian [25]. CNN learning-based approaches usually build coarse-to-fine deep learning architectures such as [49], where CNN blocks simulate iterative optimization, or [53] which deblurs the image using a scale-recurrent network. The task

becomes much more complex when the blur varies spatially. Early approaches decompose the spatially-varying blur into a finite basis of spatially-uniform blur kernels and their respective spatially-varying weights [41]. This approach drastically reduces the dimension of the blur operator and makes it computable in a reasonable amount of time using Fourier transform. [37] build an alternative model designed for faster computation and apply it to deconvolution of spatially-varying blur. More recently, [14–16] approximate the spatially-varying blur operator in the wavelet basis by a diagonal or sparse operator. Their decomposition allows very efficient computation of the blur operator and its transpose since the structure of the operator allows GPU parallelization. Other approaches such as [12] use HQS splitting to decouple the prior and data term. The data step is computed using an approximation of the inverse blur and the prior step is solved using CNN priors. Finally, jointly solving the non-uniform deblurring and upsampling (super-resolution) problem is a much more challenging task that has been much less studied [8]

3 Model

3.1 Problem Formulation

The standard model for single-image super-resolution with multiple degradations usually assumes that the low-resolution image is a blurry, noisy and subsampled version of a given high-resolution image,

$$y = (x \otimes k) \downarrow_s + \epsilon \text{ with } \epsilon \sim \mathcal{N}(0, \sigma^2), \quad (1)$$

with x the high-resolution image, y its low-resolution version, k the blur kernel, \downarrow_s the subsampling operator with scale factor s , and ϵ the noise. This formulation assumes that the blur kernel is uniform all over the image which makes the computation of the low-resolution image fast using convolution or fast Fourier transform. This assumption is not always realistic since camera or object motion will often result in non-uniform blur as illustrated in Figure 2a. In this example, background objects are moving with respect to the camera, so they appear blurry, whereas foreground objects are sharp. Spatially-varying blur can also appear when the objects are out-of-focus. In this case, the blur is closely related to the depth of field. Taking into account spatially-varying blur, the degradation model in Equation (1) replaces the convolution operator with a more general blur operator that varies across the pixels

$$y = (Hx) \downarrow_s + \epsilon \text{ with } \epsilon \sim \mathcal{N}(0, \sigma^2), \quad (2)$$

where Hx corresponds to the non-uniform blur operator applied to image x (flattened as a column vector). Working with unconstrained H leads to computationally expensive operations. In our work, the only restriction we make on H is that Hx and $H^T x$ must be computed in a reasonable amount of time. A basic example for such a use case is the O’Leary model [41] where H is decomposed as a linear combination

$$H = \sum_{i=1}^P U_i K_i \quad (3)$$



(a) Example of spatially-varying blur.

Article	SR	UB	SVB	MB	Blind
Bicubic	✓	✗	✗	✗	✓
ESRGAN [57]	✓	✗	✗	✗	✓
BSRGAN [62]	✓	✓	✗	✗	✓
SwinIR [28]	✓	✓	✗	✗	✓
IKC [20]	✓	✓	✗	✗	✓
BlindSR [8]	✓	✓	✓	✗	✓
ZSSR [50]	✓	✓	✗	✗	✗
DualSR [13]	✓	✓	✗	✗	✓
USRNet [63]	✓	✓	✗	✓	✗
Architecture	SR	UB	SVB	MB	Blind
RRDB [57]	✓	✓	(✓)	(✓)	✓
SwinIR [28]	✓	✓	(✓)	(✓)	✓
SFTMD + PCA [20]	✓	✓	✓	(✗)	✗
BlindSR [8]	✓	✓	✓	(✗)	✗
Ours	✓	✓	✓	✓	✗

(b) Method comparison table.

Figure 2: (a) Background objects are moving with respect to the camera, so they appear blurry, whereas foreground objects are sharp. (b) Restoration problems that *are addressed by previous articles* or that *can be potentially solved by available architectures*: SR=single image Super-Resolution; UB = Uniform Blur; SVB = Spatially Varying Blur; MB = Motion Blur. Brackets stand for potential use case of the architecture that have not been tested in the literature to our knowledge.

of uniform blur (convolution) operators K_i with spatially varying mixing coefficients, *i.e.* diagonal matrices U_i such that $\sum_{i=1}^P U_i = Id$, $U_i \geq 0$. This model provides a convenient approximation of a spatially-varying blur operator, by reducing both the memory and computing resources required to store and compute this operator. In practice, K_i may represent a basis of different kinds of (defocus or motion) blur, and the U_i can represent object segmentation masks or sets of pixels with similar blur kernels.

3.2 Deep Plug-and-Play

Model-based variational or Bayesian methods usually solve the SISR problem in Equation (2) by imposing a prior with density $p(x) \propto e^{-\lambda\Phi(x)}$ to the HR image x (common choices for Φ are Total Variation or ℓ_1 norm of wavelet coefficients). Then the maximization of the posterior density $p(x|y) \propto p(y|x)p(x)$ leads to the following optimization problem to compute the MAP estimator:

$$x^* = \arg \min_x \frac{1}{2\sigma^2} \|(Hx) \downarrow_s - y\|_2^2 + \lambda\Phi(x). \quad (4)$$

This family of optimization problems is often solved using iterative alternate minimization schemes, like ADMM [3], which leads to iterating the following steps for $k = 0, \dots, N$:

$$x_{k+1} = \arg \min_x \lambda\Phi(x) + \frac{\mu}{2} \|x - (v_k - u_k)\|_2^2 = \mathcal{P}_{\sqrt{\lambda/\mu}}(v_k - u_k) \quad (5)$$

$$v_{k+1} = \arg \min_v \frac{1}{2\sigma^2} \|(Hv) \downarrow_s - y\|_2^2 + \frac{\mu}{2} \|v - (x_{k+1} - u_k)\|_2^2 \quad (6)$$

$$u_{k+1} = u_k + (x_{k+1} - v_{k+1}). \quad (7)$$

For convex Φ this is known to converge to the solution of Equation (4) as $k \rightarrow \infty$. Deep plug-and-play methods use more sophisticated (possibly non-convex) learned regularizers by simply replacing the regularization step in Equation (5), by a CNN denoiser \mathcal{P}_β which was pretrained to remove zero-mean Gaussian noise with variance β^2 . The convergence of the iterative plug-and-play ADMM scheme still holds in this non-convex case for careful choices of the denoiser and the hyperparameters (λ, μ) [47].

In the case of a uniform blur, the z -update can be efficiently computed using the fast Fourier transform [63, 66] since the operator H is diagonal in the Fourier basis. However, this is no longer the case for spatially-varying blur. Even for simpler use cases such as the O’Leary model from Equation (3) solving the subproblem (6) can be very computationally expensive. To avoid this, linearized ADMM [43, sec 4.4.2] (see also [17, 32, 42, 65]) substitutes the splitting variable v by $z = Hv$, and replace the quadratic term $\|Hx - z_k\|^2$ by $\rho(H^T Hx_k - H^T z_k)^T x + \frac{\rho}{2}\|x - x_k\|^2$ in the x -update, in order to avoid the need to invert H . This term correspond to a linearization of the quadratic term with an extra regularization $\frac{\rho}{2}\|x - x_k\|^2$ that controls the distance to the point of application of the linearization. As a consequence, Equations (5) to (7) are rewritten as follows:

$$x_{k+1} = \arg \min_x \lambda \Phi(x) + \frac{\mu}{2} \|x - (x_k - (\rho\mu)H^T(Hx_k - z_k + u_k))\|_2^2 \quad (8)$$

$$= \mathcal{P}_{\sqrt{\lambda/\mu}}(x_k - (\rho\mu)H^T(Hx_k - z_k + u_k))$$

$$z_{k+1} = \arg \min_z \frac{1}{2\sigma^2} \|z \downarrow_s - y\|_2^2 + \frac{\rho}{2} \|z - (Hx_{k+1} + u_k)\|_2^2 \quad (9)$$

$$u_{k+1} = u_k + Hx_{k+1} - z_{k+1}, \quad (10)$$

with μ, ρ hyper-parameters of the optimization scheme.

Now Equation (9) can be easily computed in closed form since it does not require to invert a matrix involving H anymore (see Section B of the Appendix for more information). We have:

$$z_{k+1}(i, j) = \frac{((y \uparrow_s) + \sigma^2 \rho(Hx_{k+1} + u_k))(i, j)}{\sigma^2 \rho + \delta_{i \equiv 0 \pmod{s}} \delta_{j \equiv 0 \pmod{s}}}, \quad (11)$$

where $(.) \uparrow_s$ corresponds to the zero-padding up-sampling with scale factor s and $\delta_{i \equiv 0 \pmod{s}} \delta_{j \equiv 0 \pmod{s}}$ is the indicator function that is equal to 1 on the pixels divided by the scale factor and 0 otherwise. The whole deep plug-and-play iterative program is summarized in Algorithm 1. The linearized ADMM algorithm in Equations (8) to (10) was not yet studied in the Plug & Play context, but recent results in [33] and [19] suggest that it actually converges for some careful choices of the parameters λ, μ, ρ (see Section A of the Appendix for details). These theoretical results motivated the Unfolded version of the linearized PnP-ADMM algorithm that we present in the next section, and is the basis of the experimental results in Section 4.

3.3 Deep Unfolding Networks

Deep plug-and-play methods achieve impressive performance on image restoration tasks. However, their efficiency highly relies on the choice of their hyper-parameters. Finding correct values for the latter can be challenging. These methods also require a sufficient number of steps to

Algorithm 1 Deep Plug-and-Play Linearized ADMM algorithm

Solves $x = \arg \min_x \frac{1}{\sigma^2} \|(Hx) \downarrow_s - y\|^2 + \lambda \Phi(x)$

using denoiser $\mathcal{P}_\beta = \text{prox}_{\beta^2 \Phi}$ as an implicit regularizer.

Input: Measurements y , spatially varying kernel H , scale factor s , noise level σ , number of iterations N , hyper-parameters λ, μ, ρ

Output: super-resolved, deconvolved and denoised image x_N

$$x_0 \leftarrow y \uparrow_s$$

$$z_0 \leftarrow Hx_0$$

$$u_0 \leftarrow 0$$

for $k \in [0, N - 1]$ **do**

$$x_{k+1} = \mathcal{P}_{\sqrt{\lambda/\mu}}(x_k - (\mu\rho)H^T(Hx_k - z_k + u_k))$$

$$z_{k+1}(i, j) = \frac{((y \uparrow_s) + \sigma^2 \rho(Hx_{k+1} + u_k))(i, j)}{\sigma^2 \rho + \delta_{i \equiv 0 \pmod{s}} \delta_{j \equiv 0 \pmod{s}}}$$

$$u_{k+1} = u_k + Hx_{k+1} - z_{k+1}$$

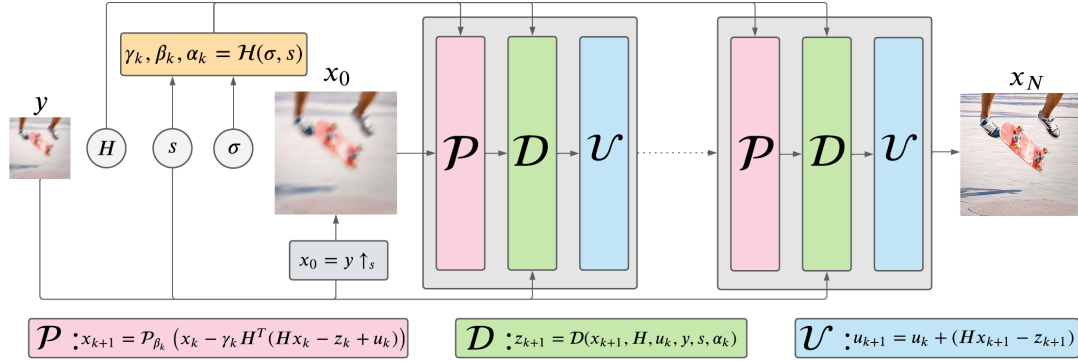


Figure 3: Model architecture, the low-resolution image is upsampled and alternately fed to the prior module \mathcal{P} , the data module \mathcal{D} and the update module \mathcal{U} during N iterations

properly converge which is time-consuming. We improve the runtime and simplify the hyper-parameter tuning process by unfolding our algorithm into a deep learning architecture. This architecture is composed of a fixed and small number of iterations of the linearized ADMM algorithm and a MLP that automatically selects the hyper-parameters. The whole network is optimized using end-to-end training. Following the linearized ADMM formulation, the architecture alternates between a prior-enforcing step \mathcal{P} corresponding to Equation (8), a data-fitting step \mathcal{D} (see Equation (9)) and finally an update block \mathcal{U} (see Equation (10)). These blocks are respectively stacked N times corresponding to the number of iterations. The optimization process requires the hyper-parameter triplets (λ, μ, ρ) that are predicted by the hyper-parameters block \mathcal{H} at each step. The resulting architecture of our deep-unfolding network is presented in Figure 3. Next, we present each block in detail.

The first block of our network is the prior module \mathcal{P} . As explained in Section 3.2, Equation (8) corresponds to a denoising problem, that is approximated by a CNN denoiser. Based on the work in [63], we use a ResUNet [10] architecture with the denoising level as an extra input for \mathcal{P} . All the parameters of the ResUNet are learned during the end-to-end training process. Retraining the parameters of the network helps to obtain the best quality results for the given number of iterations. The x -update is finally expressed as:

$$x_{k+1} = \mathcal{P}_{\beta_k} (x_k - \gamma_k H^T (H x_k - z_k + u_k)), \quad (12)$$

with $\beta_k = \sqrt{\lambda_k / \mu_k}$ and $\gamma_k = \mu_k \rho_k$. The splitting algorithm introduces the quantity $x_k - \gamma_k H^T (H x_{k+1} - z_k + u_k)$. This quantity can be interpreted as a deblurring gradient descent step on the current clean estimate x_k . The x -update combines the deblurring and denoising operations.

The data-term module \mathcal{D} computes the proximal operator of $z \mapsto \frac{1}{2\sigma^2} \|z \downarrow_s - y\|_2^2$ at $z = H x_{k+1} + u_k$. Following Equation (11), we re-write our data-term as:

$$z_{k+1} = \mathcal{D}(x_{k+1}, H, u_k, y, s, \alpha_k), \quad (13)$$

with $\alpha_k = \sigma^2 \rho_k$. The data term will ensure that our current estimate of the sharp image is consistent with the degraded input. It also acts as a mechanism of injection of the degraded image y through the iterations.

The update module \mathcal{U} updates the dual variable (or Lagrange multiplier) u of the ADMM algorithm. This block does not have trainable parameters. We decided to integrate this step into the architecture to be consistent with the ADMM formulation.

Finally, the $(\gamma_k, \beta_k, \alpha_k)$ hyper-parameters of the plug-and-play model are predicted as a function of noise level σ and scale factor s by a neural network \mathcal{H} . Indeed $\alpha_k = \sigma^2 \rho_k$ directly depends on σ and $\beta_k = \sqrt{\lambda_k / \mu_k}$ depends on the regularization parameter λ whose optimal value is usually affected by both σ and s . For the architecture of \mathcal{H} , we use 3 fully connected layers with ReLU activations. The dimension of the hidden layers is 64.



Figure 4: Example of data generated by our pipeline

3.4 Training

The architecture is trained end-to-end using the L1 loss for 200 epochs. We start with a learning rate of $1e-4$ and decrease it every 50 epochs by a factor 0.1. The ResUNet parameters were initialized by a pre-trained model that solves a Gaussian denoising problem. We found that doing so improves the stability of the model during training. We use $N=8$ iterations in our unfolded architecture for the experiments. The network is trained using scale factors $s \in \{1, 2, 3, 4\}$, noise levels $\sigma \in [0, 25]$ and spatially varying blur kernels composed various motion blurs and Gaussian blurs.

4 Experiments

4.1 Data Generation

Gathering real-world data with spatially-varying blur and their respective kernels is very complicated. Instead, we train our model using synthetic data. For this experiment, we adopted the O’Leary blur model from Equation (3). This blur decomposition covers a large variety of spatially-varying blurs ranging from motion blur to defocus blur. Figure 4 represents an example of synthetic blur obtained using this formulation. For the training and testing, we used COCO dataset [31]. COCO dataset is a well-known large-scale dataset for object detection, segmentation, and image captioning. It is composed of more than 200K images segmented for 80 object categories and 91 stuff categories representing 1.5 million object instances. We use the segmentation masks to blur the objects and the background. We use both Gaussian kernels and motion blur kernels. We build a database of motion blur kernels using [18]. To ensure a smooth and realistic transition between the blurred areas, we blur the borders of the masks so that a mix between blurs occurs at the edges of the objects. We finally normalize the masks so that their sum is equal to 1 for each pixel. After blurring the image, we apply nearest neighbor downsampling with scale factor varying in $\{1, 2, 3, 4\}$ and Gaussian blur with $\sigma \in [0, 25]$.

Finally, our data generation pipeline implements the following degradation model:

$$y = \left(\sum_{i=1}^P U_i K_i x \right) \downarrow_s + \epsilon, \quad (14)$$

with x the clean image, y its low-resolution version, s the scale factor, and ϵ the noise.

4.2 Compared Methods

We compare the proposed model to Bicubic upsampling (widely used baseline), RRDB [57], SwinIR [28], SFTMD [20], BlindSR [8] and USRNet [63].

Few super-resolution models can generalize to non-uniform blur (see Table 2b). We believe that the models listed above represent the current most pertinent solutions for such a setting. However, using the pre-trained weights from the source code of each model leads to poor performance on our testing dataset since they are trained using uniform blur kernels. In order to ensure a fair comparison with our model, we retrain all those architectures on our database. We use the MSE loss for the retraining of all models so that the PSNR is maximized. Next, we present in details how we use those architectures.

RRDB and SwinIR described in section 2.1 are blind methods so we just retrain them on our dataset using the configuration given by the authors.

SFTMD is the non-blind architecture introduced in [20] that combines kernel encoding using Principal Components Analysis (PCA) and spatial features transforms (SFT) [56] layers. The PCA-encoded blur kernel is fed to the SFT-based network along with the low-resolution image. In the case of spatially-varying blur, they encode the kernels at each pixel’s location and give the resulting spatially-varying map of encoded kernels to the network.

BlindSR proposes an alternative to the PCA for the encoding of the kernel. They use an MLP that is trained along with the super-resolution network. This allows the network to encode more complex kernels. We use the non-blind part of BlindSR that is composed of a backbone with convolutions, dense layers and residual connections with MLP encoding for the kernel.

We finally compare our architecture to USRNet, which is similar to our model but works only with uniform blur. Since we work with the O’Leary model (3), we can apply USRNet on each blurred mask U_i with their corresponding uniform blur kernel K_i and then reconstruct the results by summing the output of the model on each mask. Since we work with the classical USRNet, we do not retrain it and use the weights from the source code of the method. *i.e.* $\text{USRNet}(y, H) \approx \sum_{i=1}^P U_i \text{USRNet}(y, K_i)$

4.3 Quantitative Results

Table 1 summarizes the PSNR, SSIM (structural similarity index) and LPIPS (learned perceptual image patch similarity) on the different testsets. The testsets are constructed from the COCO validation set and the degradation model of Equation 14. Performance on Gaussian and motion blur are evaluated separately. We test the models on x2 and x4 super-resolution without additive noise.

Firstly, non-blind models outperform blind ones by a large margin. The extra information about the degradation is well used by the networks. The blind transformers-based architecture of SwinIR is more efficient than the classical RRDB. For the non-blind architectures, we can see the importance of how the blur operator information is given to the network. Specifically, the neural network encoding of the blur operator from BlindSR outmatches by far the PCA encoder from the IKC version of SFTMD. It highlights the fact that the PCA model is not complex enough to capture the interesting features of the blur kernels. BlindSR model performs well on the Gaussian testset but fails to generalize on motion blur. One reason for that is the fact that motion

Table 1: Quantitative comparison on synthetic data.

Type	Model	Gaussian testset		Motion testset	
Metrics		(PSNR↑, SSIM↑, LPIPS↓)			
	Scale	x2	x4	x2	x4
Blind	Bicubic	(22.52, 0.60, 0.57)	(21.61, 0.55, 0.60)	(21.74, 0.62, 0.39)	(20.48, 0.56, 0.57)
	RRDB [57]	(23.38, 0.67, 0.41)	(21.82, 0.57, 0.58)	(23.11, 0.65, 0.36)	(22.34, 0.60, 0.56)
	SwinIR [28]	(23.47, 0.67, 0.38)	(23.01, 0.63, 0.44)	(23.40, 0.67, 0.34)	(22.70, 0.64, 0.44)
Non-blind	SFTMD+PCA [20]	(23.76, 0.69, 0.33)	(23.12, 0.64, 0.41)	(25.15, 0.74, 0.25)	(23.97, 0.67, 0.38)
	BlindSR [8]	(26.55, 0.79, 0.24)	(25.11, 0.72, 0.34)	(26.40, 0.79, 0.20)	(24.54, 0.69, 0.35)
	USRNet [63]	(22.64, 0.74, 0.28)	(24.08, 0.72, 0.32)	(24.37, 0.75, 0.17)	(24.67, 0.72, 0.29)
	Ours	(26.59, 0.78, 0.26)	(25.37, 0.73, 0.31)	(28.20, 0.85, 0.11)	(25.36, 0.73, 0.28)

blurs are too complex to be encoded by PCA or small MLP. USRNet model reaches good SSIM and LPIPS while having low PSNR. This is mostly due to the fact that it introduces artefacts that are not captured in SSIM and LPIPS. The poor performances of USRNet underline the fact that networks trained on uniform blur cannot naively generalize well to spatially-varying blur even on simple use cases. Finally, our model outperforms all the other methods by an average of 0.15dB for the Gaussian testsets and 1.2dB on the Motion testset. It is also better on SSIM and LPIPS except for the x2 Gaussian testset where BlindSR is better.

The success of the method first relies on the fact that the kernel information does not need to be encoded to be fed to the model which allows good deblurring quality of very complex kernels. Also, the deblurring and super-resolution modules are fixed in our architecture which makes it more robust to all the blur types. It is worth pointing out that a single version of our model was used for all the scale factors without retraining.

4.4 Visual Results

Figure 5 shows some visual comparisons of the different models on scale 2 super-resolution. We excluded RRDB and SFTMD since their performance are outmatched respectively by SwinIR and BlindSR. We observe that SwinIR produces results that are still blurry. USRNet produces sharp results on the areas where the blur kernels are not mixed (*i.e.* when the area of a single degradation map is equal to one and all the other are equal to zeros) but introduces artefacts on the edges of the objects since the deblurring task is not linear. BlindSR super-resolves well the images. However, some areas remain blurry especially when there is motion blur. Finally, our model succeed to produce a sharp super-resolved image without artefacts. We observe more texture details and sharper edges.

In order to test the generalization abilities of the models, we super-resolve images with unseen blur kernels. Figure 6 shows a visual example of this experiment. The low-resolution image is blurred by two anisotropic Gaussian kernels which are applied from left to right of the image with a linear blend. We observe that BlindSR and USRNet produce artefacts. In particular, BlindSR oversharpen the numberplate and add artefacts in the grass, USRNet creates artefacts everywhere. SwinIR result does not have artefact but the image is still blurry. Finally, our model produces sharp edges on the numberplate while keeping the grass without artefacts. The

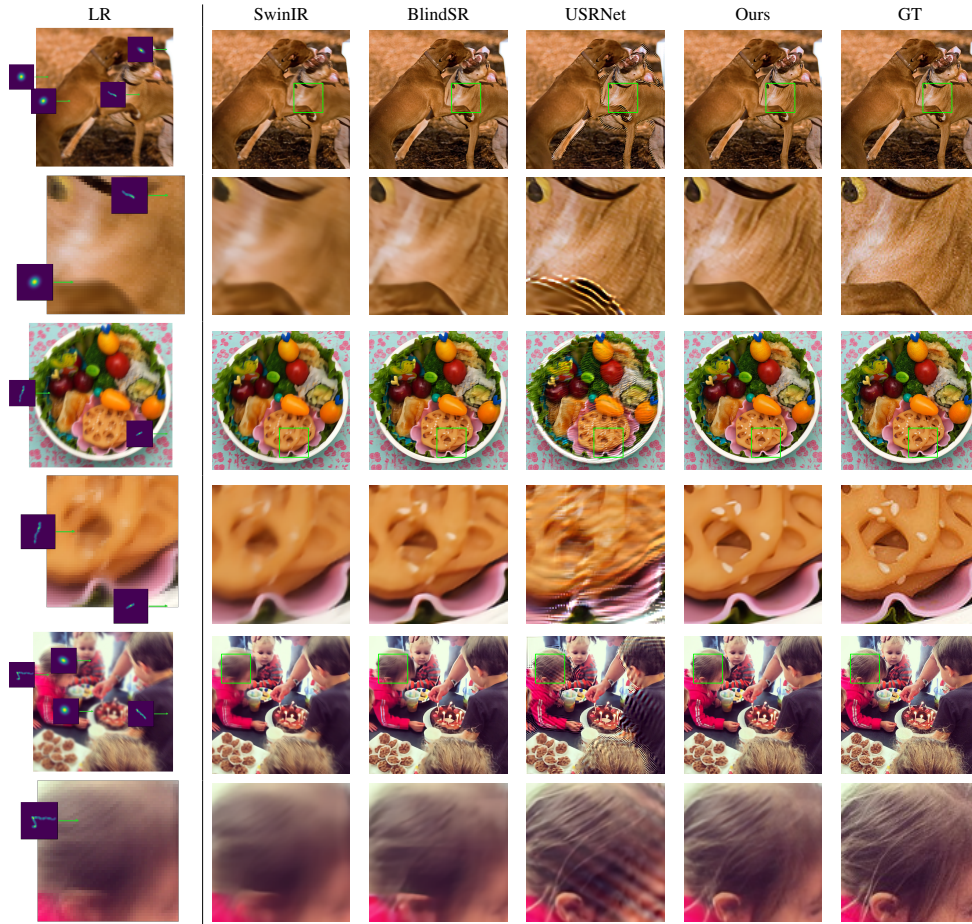


Figure 5: Visual comparison of the super-resolution performance of the models with a scale factor of 2. The different blur kernels are displayed in the LR images.



Figure 6: Performance of the models on unseen kernels, instead of using binary masks, the weights U_i (in color) vary linearly from left to right between two symmetrical blur kernels K_i (in grayscale).

deblurring step of our model is fixed so it is not affected with unseen kernels. This characteristic can be very useful for practical applications. More visual results can be found in Section C of the Appendix.

4.5 Study of the Algorithm

In this section, we analyze the behavior of our unfolding algorithm and draw parallel to regular plug-and-play methods. Figure 7 highlights the hyper-parameters predicted by our hyper-parameters network \mathcal{H} for different scale factors and the behavior of the model at different steps. We first observe that the pre-trained MMSE denoiser contained in the \mathcal{D} module no longer behave as MMSE denoiser but more as an artefacts cleaner. Consequently, the β parameters that is fed to the denoiser no longer acts as the noise level to be removed but more as slider that remove more artefacts as it grows bigger. The hyper-parameters predictor network $\mathcal{H}(\sigma, s)$ learns a coarse to fine strategy. Specifically, in Figure 7b, the β corresponding to the artefacts removal intensity decrease along with the iterations. On the other side, in Figure 7c, γ which controls the step size of the deblurring gradient descent from Equation 8 starts from a high value and linearly decreases through the iterations. Finally, in Figure 7a, α (which is inversely proportional to the quantity of the low-resolution image that is re-injected to the current super-resolution estimation) increases exponentially. It means that the closer we are to the final step, the less we inject the low-resolution to the current super-resolution estimate. Those strategy are very popular in deep plug-and-play applications, the main advantage of our deep unfolding architecture is that they were optimized for the task we targeted by end-to-end training instead of being manually tuned.

5 Conclusion & Future Research

In this paper, we approach the problem of single-image super-resolution with spatially-varying blur. We propose a deep unfolding architecture that handles various blur kernels, scale factors, and noise levels. Our unfolding architecture derives from a deep plug-and-play algorithm based on the linearized ADMM splitting technique. Our architecture inherits both from the flexibil-

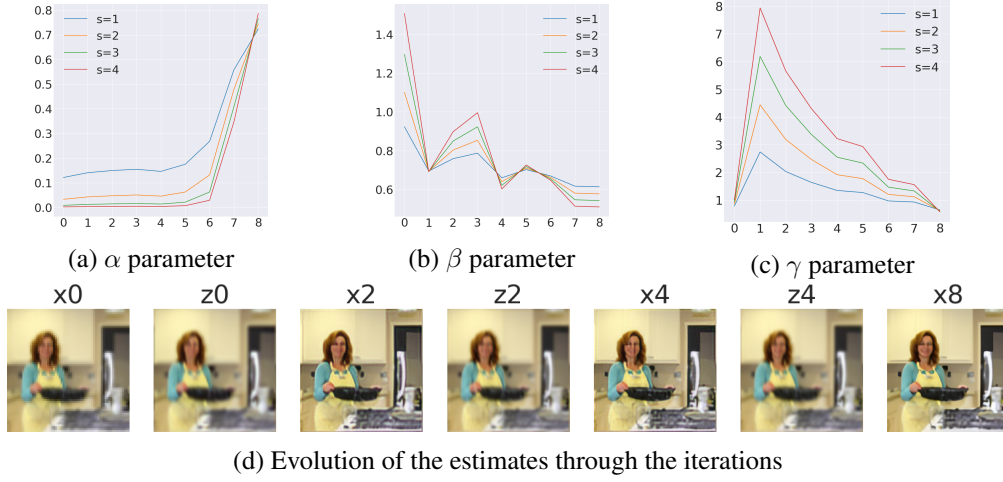


Figure 7: This figure displays the hyper-parameters predicted by $\mathcal{H}(\sigma, s)$ for different SR scale factors (s), $\sigma = 10$ and iterations $k \in \{1, \dots, 8\}$. We also show the evolution of the intermediate estimates through the iterations (see Fig. 3).

ity of plug-and-play algorithms and from the speed and efficiency of learning-based methods through end-to-end training. Experimental results using the O’Leary blur model highlight the superiority of the proposed method in terms of performance and generalization. The study of other spatially-varying blur models along with the blind setting is left for future work. In particular we intend to build a blind model by combining our approach with a local blur estimation module [6, 29].

References

- [1] Andrés Almansa, Sylvain Durand, and Bernard Rougé. Measuring and Improving Image Resolution by Adaptation of the Reciprocal Cell. *Journal of Mathematical Imaging and Vision*, 21(3):235–279, nov 2004.
- [2] Sefi Bell-Kligler, Assaf Shocher, and Michal Irani. Blind super-resolution kernel estimation using an internal-gan. In *NeurIPS*, 2019.
- [3] Stephen Boyd, Neal Parikh, Eric Chu, Borja Peleato, and Jonathan Eckstein. Distributed Optimization and Statistical Learning via the Alternating Direction Method of Multipliers. *Foundations and Trends® in Machine Learning*, 3(1):1–122, 2010.
- [4] Alon Brifman, Yaniv Romano, and Michael Elad. Turning a denoiser into a super-resolver using plug and play priors. In *2016 IEEE International Conference on Image Processing (ICIP)*, 2016.

- [5] Gregory T. Buzzard, Stanley H. Chan, Suhas Sreehari, and Charles A. Bouman. Plug-and-play unplugged: Optimization-free reconstruction using consensus equilibrium. *SIAM Journal on Imaging Sciences*, 2018.
- [6] Guillermo Carbajal, Patricia Vitoria, Mauricio Delbracio, Pablo Musé, and José Lezama. Non-uniform blur kernel estimation via adaptive basis decomposition. *arXiv:2102.01026*, 2021.
- [7] Stanley H. Chan, Xiran Wang, and Omar A. Elgandy. Plug-and-play admm for image restoration: Fixed-point convergence and applications. *IEEE Transactions on Computational Imaging*, 2017.
- [8] Victor Cornillère, Abdelaziz Djelouah, Wang Yifan, Olga Sorkine-Hornung, and Christopher Schroers. Blind image super-resolution with spatially variant degradations. In *ACM Transactions on Graphics*, 2019.
- [9] Yehuda Dar, Alfred M. Bruckstein, Michael Elad, and Raja Giryes. Postprocessing of compressed images via sequential denoising. *IEEE Transactions on Image Processing*, 2016.
- [10] Foivos I. Diakogiannis, François Waldner, Peter Caccetta, and Chen Wu. Resunet-a: A deep learning framework for semantic segmentation of remotely sensed data. *ISPRS Journal of Photogrammetry and Remote Sensing*, 162:94–114, 2020.
- [11] Chao Dong, Chen Change Loy, Kaiming He, and Xiaoou Tang. Learning a deep convolutional network for image super-resolution. In David Fleet, Tomas Pajdla, Bernt Schiele, and Tinne Tuytelaars, editors, *Proceedings of European Conference on Computer Vision (ECCV)*, pages 184–199. Springer International Publishing, 2014.
- [12] Thomas Eboli, Jian Sun, and Jean Ponce. End-to-end interpretable learning of non-blind image deblurring. In *ECCV*, 2020.
- [13] Mohammad Emad, Maurice Peemen, and Henk Corporaal. DualSR: Zero-Shot Dual Learning for Real-World Super-Resolution. In *2021 IEEE Winter Conference on Applications of Computer Vision (WACV)*, pages 1629–1638, 2021.
- [14] Paul Escande and Pierre Weiss. Accelerating l1-l2 deblurring using wavelet expansions of operators. *Journal of Computational and Applied Mathematics*, 343:373–396, dec 2018.
- [15] Paul Escande, Pierre Weiss, and François Malgouyres. Image restoration using sparse approximations of spatially varying blur operators in the wavelet domain. *Journal of Physics: Conference Series*, 464(1):012004, oct 2013.
- [16] Paul Escande, Pierre Weiss, and François Malgouyres. Spatially varying blur recovery. diagonal approximations in the wavelet domain. *ICPRAM*, 2013.
- [17] Ernie Esser, Xiaoqun Zhang, and Tony F. Chan. A general framework for a class of first order primal-dual algorithms for convex optimization in imaging science. In *Society for Industrial and Applied Mathematics (SIAM)*, 2010.

- [18] Fabien Gavant, Laurent Alacoque, Antoine Dupret, and Dominique David. A physiological camera shake model for image stabilization systems. In *SENSORS, 2011 IEEE*, pages 1461–1464, 2011.
- [19] Rémi Gribonval. Should penalized least squares regression be interpreted as maximum a posteriori estimation? *IEEE Transactions on Signal Processing*, 59(5):2405–2410, 2011.
- [20] Jinjin Gu, Hannan Lu, Wangmeng Zuo, and Chao Dong. Blind super-resolution with iterative kernel correction. In *2019 IEEE/CVF Conference on Computer Vision and Pattern Recognition (CVPR)*, pages 1604–1613, 2019.
- [21] Felix Heide, Markus Steinberger, Yun-Ta Tsai, Mushfique Rouf, Dawid Pajak, Dikpal Reddy, Orazio Gallo, Jing Liu, Wolfgang Heidrich, Karen Egiazarian, Jan Kautz, and Kari Pulli. FlexISP: A Flexible Camera Image Processing Framework. *ACM Transactions on Graphics*, 33, 2014.
- [22] Ulugbek S. Kamilov, Hassan Mansour, and Brendt Wohlberg. A plug-and-play priors approach for solving nonlinear imaging inverse problems. *IEEE Signal Processing Letters*, 2017.
- [23] Jiwon Kim, Jung Kwon Lee, and Kyoung Mu Lee. Accurate image super-resolution using very deep convolutional networks. In *2016 IEEE Conference on Computer Vision and Pattern Recognition (CVPR)*, pages 1646–1654, 2016.
- [24] Jiwon Kim, Jung Kwon Lee, and Kyoung Mu Lee. Deeply-recursive convolutional network for image super-resolution. In *2016 IEEE Conference on Computer Vision and Pattern Recognition (CVPR)*, pages 1637–1645, 2016.
- [25] Dilip Krishnan and Rob Fergus. Fast image deconvolution using hyper-laplacian priors. In Y. Bengio, D. Schuurmans, J. Lafferty, C. Williams, and A. Culotta, editors, *Advances in Neural Information Processing Systems*, volume 22. Curran Associates, Inc., 2009.
- [26] Rémi Laumont, Valentin de Bortoli, Andrés Almansa, Julie Delon, Alain Durmus, and Marcelo Pereyra. On Maximum-a-Posteriori estimation with Plug & Play priors and stochastic gradient descent. Technical report, MAP5, jan 2022.
- [27] Anat Levin, Yair Weiss, Fredo Durand, and William T. Freeman. Understanding and evaluating blind deconvolution algorithms. In *2009 IEEE Conference on Computer Vision and Pattern Recognition*, pages 1964–1971, 2009.
- [28] Jingyun Liang, Jiezhong Cao, Guolei Sun, Kai Zhang, Luc Van Gool, and Radu Timofte. Swinir: Image restoration using swin transformer. In *2021 IEEE/CVF International Conference on Computer Vision Workshops (ICCVW)*, pages 1833–1844, 2021.
- [29] Jingyun Liang, Guolei Sun, Kai Zhang, Luc Van Gool, and Radu Timofte. Mutual affine network for spatially variant kernel estimation in blind image super-resolution. In *IEEE International Conference on Computer Vision (ICCV)*, 2021.

- [30] Bee Lim, Sanghyun Son, Heewon Kim, Seungjun Nah, and Kyoung Mu Lee. Enhanced deep residual networks for single image super-resolution. In *2017 IEEE Conference on Computer Vision and Pattern Recognition Workshops (CVPRW)*, pages 1132–1140, 2017.
- [31] Tsung-Yi Lin, Michael Maire, Serge Belongie, Lubomir Bourdev, Ross Girshick, James Hays, Pietro Perona, Deva Ramanan, C. Lawrence Zitnick, and Piotr Dollár. Microsoft COCO: Common Objects in Context. In *(ECCV) European Conference on Computer Vision*, 2015.
- [32] Zhouchen Lin, Risheng Liu, and Zhixun Su. Linearized alternating direction method with adaptive penalty for low-rank representation. In *Advances in Neural Information Processing Systems*. Curran Associates, Inc., 2011.
- [33] Qinghua Liu, Xinyue Shen, and Yuantao Gu. Linearized ADMM for Nonconvex Nonsmooth Optimization With Convergence Analysis. *IEEE Access*, 7:76131–76144, 2019.
- [34] Ze Liu, Yutong Lin, Yue Cao, Han Hu, Yixuan Wei, Zheng Zhang, Stephen Lin, and Baining Guo. Swin transformer: Hierarchical vision transformer using shifted windows. In *International Conference on Computer Vision (ICCV)*, 2021.
- [35] F Malgouyres and F Guichard. Edge Direction Preserving Image Zooming: A Mathematical and Numerical Analysis. *SIAM Journal on Numerical Analysis*, 39(1):1–37, jan 2001.
- [36] Tim Meinhardt, Michael Moeller, Caner Hazirbas, and Daniel Cremers. Learning Proximal Operators: Using Denoising Networks for Regularizing Inverse Imaging Problems. In *(ICCV) International Conference on Computer Vision*, pages 1799–1808. IEEE, oct 2017.
- [37] Hirsch Michael, Sra Suvrit, Schölkopf Bernhard, and Harmeling Stefan. Efficient filter flow for space-variant multiframe blind deconvolution. In *IEEE Computer Society Conference on Computer Vision and Pattern Recognition*, 2010.
- [38] Tomer Michaeli and Michal Irani. Nonparametric Blind Super-resolution. In *(ICCV) International Conference on Computer Vision*, pages 945–952. IEEE, dec 2013.
- [39] Tomer Michaeli and Michal Irani. Blind Deblurring Using Internal Patch Recurrence. In *(ECCV) European Conference on Computer Vision*, volume 8691 LNCS, pages 783–798. Springer, 2014.
- [40] Peyman Milanfar, editor. *Super-Resolution Imaging*. CRC Press, dec 2011.
- [41] James G. Nagy and Dianne P. O’Leary. Restoring images degraded by spatially variant blur. *SIAM Journal on Scientific Computing*, 19(4):1063–1082, 1998.
- [42] Hua Ouyang, Niao He, and Alexander Gray. Stochastic ADMM for Nonsmooth Optimization. *arXiv:1211.0632*, nov 2012.
- [43] Neal Parikh and Stephen Boyd. Proximal Algorithms. *Foundations and Trends® in Optimization*, 1(3):127–239, 2014.

- [44] Matan Protter, Michael Elad, Hiroyuki Takeda, and Peyman Milanfar. Generalizing the nonlocal-means to super-resolution reconstruction. In *IEEE Transactions on Image Processing*, volume 18, pages 36–51, jan 2009.
- [45] Yaniv Romano, John Isidoro, and Peyman Milanfar. RAISR: Rapid and Accurate Image Super Resolution. *IEEE Transactions on Computational Imaging*, 3(1):110–125, jun 2016.
- [46] Leonid I. Rudin, Stanley Osher, and Emad Fatemi. Nonlinear total variation based noise removal algorithms. *Physica D: Nonlinear Phenomena*, 60(1):259–268, 1992.
- [47] Ernest Ryu, Jialin Liu, Sicheng Wang, Xiaohan Chen, Zhangyang Wang, and Wotao Yin. Plug-and-play methods provably converge with properly trained denoisers. In Kamalika Chaudhuri and Ruslan Salakhutdinov, editors, *Proceedings of the 36th International Conference on Machine Learning*, volume 97 of *Proceedings of Machine Learning Research*, pages 5546–5557, Long Beach, California, USA, 09–15 Jun 2019. PMLR.
- [48] Chitwan Saharia, Jonathan Ho, William Chan, Tim Salimans, David J. Fleet, and Mohammad Norouzi. Image Super-Resolution via Iterative Refinement. *arXiv:2104.07636*, 2021.
- [49] Christian J. Schuler, Michael Hirsch, Stefan Harmeling, and Bernhard Schölkopf. Learning to deblur. *IEEE Transactions on Pattern Analysis and Machine Intelligence*, 38(7):1439–1451, 2016.
- [50] Assaf Shocher, Nadav Cohen, and Michal Irani. Zero-shot super-resolution using deep internal learning. In *2018 IEEE/CVF Conference on Computer Vision and Pattern Recognition*, pages 3118–3126, 2018.
- [51] Michal Šorel, Filip Šroubek, and Jan Flusser. Towards Super-Resolution in the Presence of Spatially Varying Blur. In *Super-Resolution Imaging*, chapter 7, pages 187–218. CRC Press, dec 2017.
- [52] Ying Tai, Jian Yang, Xiaoming Liu, and Chunyan Xu. Memnet: A persistent memory network for image restoration. In *2017 IEEE International Conference on Computer Vision (ICCV)*, pages 4549–4557, 2017.
- [53] Xin Tao, Hongyun Gao, Xiaoyong Shen, Jue Wang, and Jiaya Jia. Scale-recurrent network for deep image deblurring. In *2018 IEEE/CVF Conference on Computer Vision and Pattern Recognition*, pages 8174–8182, 2018.
- [54] Tom Tirer and Raja Giryes. Image restoration by iterative denoising and backward projections. *IEEE Transactions on Image Processing*, 2019.
- [55] Singanallur V. Venkatakrishnan, Charles A. Bouman, and Brendt Wohlberg. Plug-and-play priors for model based reconstruction. *IEEE Global Conference on Signal and Information Processing*, 2013.
- [56] Xintao Wang, Ke Yu, Chao Dong, and Chen Change Loy. Recovering realistic texture in image super-resolution by deep spatial feature transform. In *2018 IEEE/CVF Conference on Computer Vision and Pattern Recognition*, pages 606–615, 2018.

- [57] Xintao Wang, Ke Yu, Shixiang Wu, Jinjin Gu, Yihao Liu, Chao Dong, Yu Qiao, and Chen Change Loy. Esrgan: Enhanced super-resolution generative adversarial networks. In *The European Conference on Computer Vision Workshops (ECCVW)*, 2018.
- [58] Xiran Wang and Stanley H. Chan. Parameter-free plug-and-play admm for image restoration. In *2017 IEEE International Conference on Acoustics, Speech and Signal Processing (ICASSP)*, 2017.
- [59] Oliver Whyte, Josef Sivic, Andrew Zisserman, and Jean Ponce. Non-uniform deblurring for shaken images. In *2010 IEEE Computer Society Conference on Computer Vision and Pattern Recognition*, pages 491–498, 2010.
- [60] Zhang Yulun, Li Kunpeng, Li Kai, Wang Lichen, Zhong Bineng, and Fu Yun. Image super-resolution using very deep residual channel attention networks. In *Proceedings of European Conference on Computer Vision (ECCV)*, 2018.
- [61] Kai Zhang, Yawei Li, Wangmeng Zuo, Lei Zhang, Luc Van Gool, and Radu Timofte. Plug-and-play image restoration with deep denoiser prior. *IEEE Transactions on Pattern Analysis and Machine Intelligence*, 2021.
- [62] Kai Zhang, Jingyun Liang, Luc Van Gool, and Radu Timofte. Designing a practical degradation model for deep blind image super-resolution. In *IEEE International Conference on Computer Vision*, pages 4791–4800, 2021.
- [63] Kai Zhang, Luc Van Gool, and Radu Timofte. Deep unfolding network for image super-resolution. In *2020 IEEE/CVF Conference on Computer Vision and Pattern Recognition (CVPR)*, pages 3214–3223, 2020.
- [64] Kai Zhang, Wangmeng Zuo, and Lei Zhang. Learning a single convolutional super-resolution network for multiple degradations. In *2018 IEEE/CVF Conference on Computer Vision and Pattern Recognition*, pages 3262–3271, 2018.
- [65] Xiaoqun Zhang, Martin Burger, and Stanley Osher. A unified primal-dual algorithm framework based on bregman iteration. In *Journal of Scientific Computing*, 2011.
- [66] Ningning Zhao, Qi Wei, Adrian Basarab, Nicolas Dobigeon, Denis Kouamé, and Jean-Yves Tournier. Fast Single Image Super-Resolution Using a New Analytical Solution for l2-l2 Problems. *IEEE Transactions on Image Processing*, vol. 25(n° 8):pp. 3683–3697, August 2016.
- [67] Xiang Zhu, Scott Cohen, Stephen Schiller, and Peyman Milanfar. Estimating spatially varying defocus blur from a single image. *IEEE Transactions on Image Processing*, 22(12):4879–4891, 2013.

A Linearized PnP ADMM

In this section, we explain some theoretical results that justify the convergence of our linearized-ADMM deep plug-and-play algorithm. In particular, we explain that our optimization problem is a particular use case of [33].

In this article, they study optimization problems of the form:

$$\min_{x,z} g(x, z) + f(x) + h(z) \quad \text{s.t.} \quad Ax + Bz = 0 \quad (15)$$

with $x \in \mathbb{R}^p$, $z \in \mathbb{R}^q$.

The Lagrangian for such problem is defined as:

$$L_\mu(x, z, u) = g(x, z) + f(x) + h(z) + \langle u, Ax + Bz \rangle + \frac{\mu}{2} \|Ax + Bz\|_2^2 \quad (16)$$

Applying the classical ADMM to the Lagrangian leads to proximal operators that can be hard and computationally expensive to compute. Instead, they propose to linearize $g(x, z) + \frac{\mu}{2} \|Ax + Bz\|_2^2$ in the $(k + 1)$ -th update leading to the linear approximation

$$\langle x - x_k, \nabla_x g(x_k, z_k) + \mu A^T (Ax_k + Bz_k) \rangle + \frac{L_x}{2} \|x - x_k\|_2^2. \quad (17)$$

They also replace $g(x, z) + h(z)$ in the $(k+1)$ -th update by its linear approximation

$$\langle z - z_k, \nabla_z g(x_{k+1}, z_k) + \nabla_z h(z_k) \rangle + \frac{L_z}{2} \|z - z_k\|_2^2. \quad (18)$$

Those linearizations lead to the following optimization algorithm:

$$x_{k+1} = \text{prox}_{f/L_x}(x_k - \frac{1}{L_x}(\nabla_x g(x_k, y_k) + A^T u_k + \beta A^T (Ax_k + Bz_k))), \quad (19)$$

$$z_{k+1} = (L_z - \mu B^T B)^{-1}(L_z z_k - \nabla_z g(x_{k+1}, z_k) - \nabla_z h(z_k) - B^T u_k - \mu B^T Ax_{k+1}), \quad (20)$$

$$u_{k+1} = u_k + \mu(Ax_{k+1} + Bz_{k+1}). \quad (21)$$

Our problem belongs to this family of optimization problems with:

- $g(x, z) = 0$,
- $f(x) = \lambda \Phi(x)$,
- $h(z) = \frac{1}{2\sigma^2} \|Sz - y\|_2^2$,
- $A = H$,
- $B = -Id$,

with S such that $Sx = x \downarrow_s$.

We easily verify that Assumption 1 from [33] is fulfilled since $g = 0$, h is quadratic and $\text{Im}(H) \subset \text{Im}(-Id) = \mathbb{R}^d$. Even if $f(x) = \lambda\Phi(x)$ is unknown in our case (we only know the denoiser \mathcal{P}_β which is *assumed* to be the proximal operator $\text{prox}_{\beta^2\Phi}$ of a certain function $\beta^2\Phi$), the work in [19] ensures the existence of such a suitable Φ , as long as \mathcal{P}_β is an MMSE denoiser. And this is (at least approximately) the case, since neural Gaussian denoisers are trained to minimize an ℓ^2 loss.

Our version of the linearized ADMM differs from [33] since we only apply the linearization in the x -update. In fact, our z -update already has a closed-form without linearization so we do not need to do an approximation. The two variants of the linearized ADMM algorithm are so similar that we expect to be able to adapt the proof of Theorem 1 in [33]. This will be the subject of future research, if needed. For the purpose of this paper, we do not strictly need such a convergence result because we do not use the *iterative* deep plug-and-play algorithm. Instead we *unfold* a fixed number of iterations to define the architecture that is trained end-to-end.

B Proximal Descent on Data-Fitting Term in Closed Form.

This section demonstrates how we get to the closed-form of the z -update. We suppose that our images x and y are vectorized (*i.e.* considered as column vectors). The dimension of x is $n \times p \times 3$ and the dimension of y is $(n/s) \times (p/s) \times 3$. Let the k -th entry of vector x denote the c_k -th channel of pixel coordinates (i_k, j_k) , *i.e.* we identify x_k in the vectorized representation with $x(i_k, j_k, c_k)$ in the image array representation. Let S be the subsampling operator seen as a matrix in the vectorized space, *i.e.* $Sx = x \downarrow_s$. The z -update is defined as the proximal operator on the data-term *i.e.*:

$$z_{k+1} = \arg \min_z \frac{1}{2\sigma^2} \|Sz - y\|_2^2 + \frac{\rho}{2} \|z - (Hx_{k+1} + u_k)\|_2^2 \quad (22)$$

$$= \arg \min_z F(z), \quad (23)$$

$F(z)$ is the sum of two quadratic functions so we use the first-order condition to find the arg min:

$$\nabla F(z) = 0 \quad (24)$$

$$\Leftrightarrow \frac{1}{\sigma^2} S^T (Sz^* - y) + \rho(z^* - (Hx_{k+1} + u_k)) = 0 \quad (25)$$

$$\Leftrightarrow (S^T S + \sigma^2 \rho Id) z^* = S^T y + \sigma^2 \rho (Hx_{k+1} + u_k). \quad (26)$$

It is worth pointing out that $(S^T S + \sigma^2 \rho Id)$ is diagonal and $S^T S$ corresponds to an entry-wise multiplication mask with ones at the sampled positions and zeros elsewhere (*i.e.* $(S^T S)_{k,k} = \mathbb{1}_{\{i_k \equiv 0 \pmod{s}\}} \mathbb{1}_{\{j_k \equiv 0 \pmod{s}\}}$).

Finally, we can rewrite Equation (26) as:

$$z^* = (S^T S + \sigma^2 \rho Id)^{-1} (S^T y + \sigma^2 \rho (Hx_{k+1} + u_k)), \quad (27)$$

Table 2: Quantitative comparison on synthetic data.

Training	Model	Gaussian testset		Motion testset	
Metrics		(PSNR↑, SSIM↑, LPIPS↓)			
	Scale	x2	x4	x2	x4
Author's weights	Bicubic	(22.52, 0.60, 0.57)	(21.61, 0.55, 0.60)	(21.74, 0.62, 0.39)	(20.48, 0.56, 0.57)
	BSRGAN [62]	(22.85, 0.65, 0.3)	(20.7, 0.54, 0.29)	(21.23, 0.61, 0.27)	(19.48, 0.53, 0.3)
	IKC [20]	None	(21.64, 0.57, 0.48)	None	(19.51, 0.54, 0.38)
	BlindSR [8]	(22.97, 0.63, 0.43)	None	(22.01, 0.64, 0.3)	None
	USRNet [63]	(22.64, 0.74, 0.28)	(24.08, 0.72, 0.32)	(24.37, 0.75, 0.17)	(24.67, 0.72, 0.29)
Retrained	RRDB [57, 62]	(23.38, 0.67, 0.41)	(21.82, 0.57, 0.58)	(23.11, 0.65, 0.36)	(22.34, 0.60, 0.56)
	SwinIR [28]	(23.47, 0.67, 0.38)	(23.01, 0.63, 0.44)	(23.40, 0.67, 0.34)	(22.70, 0.64, 0.44)
	SFTMD+PCA [20]	(23.76, 0.69, 0.33)	(23.12, 0.64, 0.41)	(25.15, 0.74, 0.25)	(23.97, 0.67, 0.38)
	BlindSR [8]	(26.55, 0.79, 0.24)	(25.11, 0.72, 0.34)	(26.40, 0.79, 0.20)	(24.54, 0.69, 0.35)
	Ours	(26.59, 0.78, 0.26)	(25.37, 0.73, 0.31)	(28.20, 0.85, 0.11)	(25.36, 0.73, 0.28)

which in the image space gives:

$$(z^*)_{i,j} = \frac{(S^T y + \sigma^2 \rho (H x_{k+1} + u_k))_{i,j}}{\sigma^2 \rho + \mathbb{1}_{\{i \equiv 0 \pmod{s}\}} \mathbb{1}_{\{j \equiv 0 \pmod{s}\}}}. \quad (28)$$

C Additional Results

In this section, we provide additional results of our model. Figure 8 shows visual results of our model on different blur kernels. The main observation here is that our model produces sharper results and more details. Also we can observe that our model remains competitive even on uniform blur kernels. Indeed, the third image is blurred by a single kernel and we can see that the performance metrics of our model is similar to those of USRNet that is one of the state-of-the-art methods for such a use case. Table 2, provides additional quantitative results on our different tests. We compare the pre-trained models provided by the source code of each method to the same models that we retrained on our dataset. Please note that the “Retrained” part of the table is the same as Table 1 in our paper.

In particular, BSRGAN [62] uses an RRDB architecture trained on DIV2K with different Gaussian blurs. IKC [20] is the blind architecture that combined SFTMD + PCA non-blind super-resolution network with a kernel refinement to find the optimal blur kernel. We also test the blind version of BlindSR [8] that is provided by the authors, unfortunately, this version is trained only using uniform blur kernels. The weights of USRNet are not re-trained in our comparison. The only difference with the author’s approach is that we apply USRNet on each mask as described in the paper. This table highlights the difficulty of doing a fair comparison between the different models of the literature. Without re-training, those models perform poorly since they are trained using uniform blur kernels. However, we believe that retraining them helps to efficiently capture the ability of the models to super-resolve images with spatially-varying blur without being biased by training data.

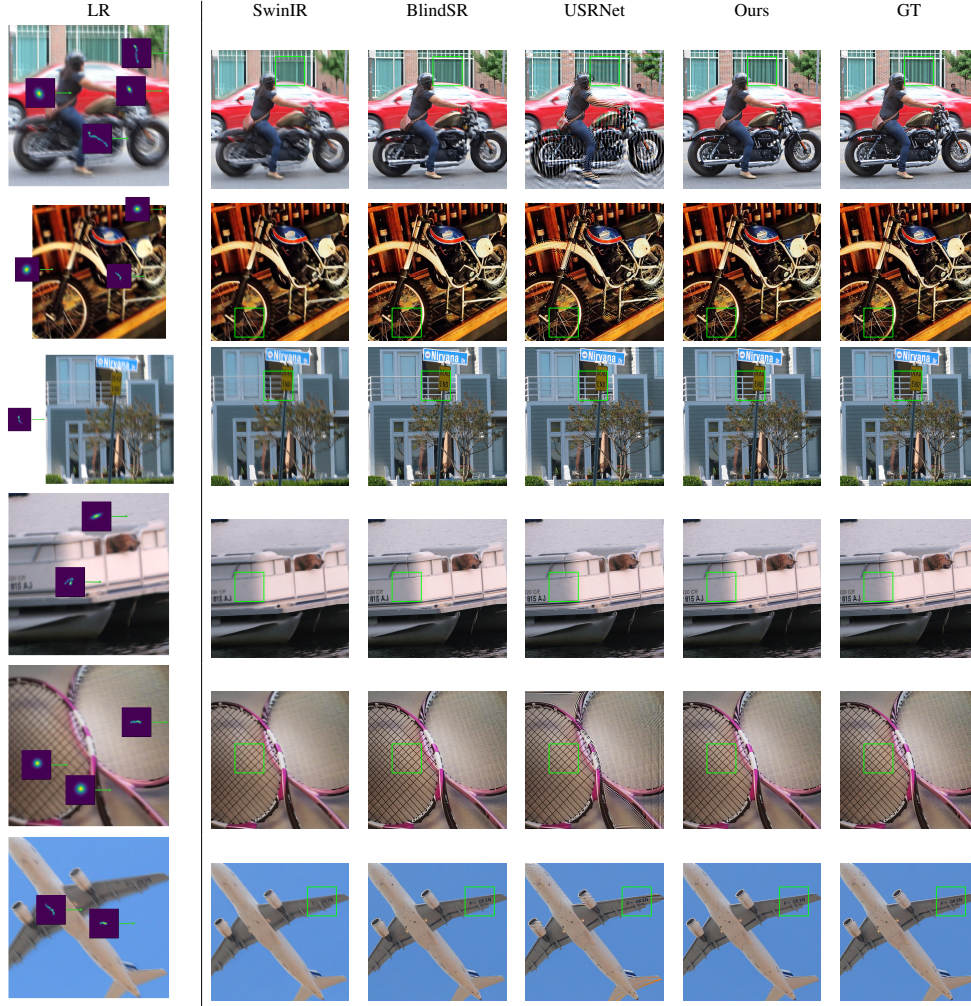


Figure 8: Visual comparison of the super-resolution performance of the models with a scale factor of 2. The different blur kernels are displayed in the LR images.